Species-Dependent Crevice Corrosion Modeling of Ni-625

Aaron Stenta,* Curtis Clemons,* Dmitry Golovaty,* Kevin Kreider,* Gerald Young,‡,* Diana Salgado,** and Scott Lillard**

ABSTRACT

A coordinated experimental and mathematical modeling effort to develop a three-stage model for determining the spatial and temporal potential, current, ionic species, and damage profiles for nickel 625 crevice corrosion applications in seawater solutions is presented. Stage one is oxygen depletion inside the crevice, stage two is the development of a critical crevice solution (induction stage), and stage three is long-term aggressive dissolution that is consistent with a nearly well-mixed, IR controlled crevice system. In stage one, deoxygenation allows separation of the anodic and cathodic sites. In stage two, local initiation occurs at the crevice tip that diffuses toward the crevice mouth. Minimal dissolution occurs in stage two and complete initiation occurs when the total anodic current is such that the critical IR drop is observed. In stage three, the crevice is saturated at or near the critical crevice solution and metal salt precipitates allow stable crevice corrosion propagation. The key inputs to the three-stage model are concentration-dependent polarization curves, and hydrolysis and hydroxide precipitation reaction data. Model calculations are compared with experimental damage histories and total current measurements. Analytical solutions and 2D modeling efforts are also used to validate the proposed 1D approach for simplified systems leading up to the complex Ni-625 system. All results agree under a thin-film approximation. Further, it is shown that with appropriate experimental input data, and knowledge from solution of the species-dependent system, a damage evolution well-mixed model provides comparable results.

KEY WORDS: crevice corrosion, critical crevice solution, damage evolution, fastener assembly, mathematical modeling, Ni-625, species-dependent

INTRODUCTION

Crevice corrosion is a corrosion mechanism that occurs in tightly confined areas that are exposed to a conductive electrolyte solution. Crevice gaps must be large enough to allow fluid penetration, yet small enough to maintain an isolated electrolyte composition. In thin crevices, the time-dependent electrolyte composition spatially isolates the anodic and cathodic regions. Along with the geometric requirement of a thin/long crevice, the bulk electrolyte must also include a system-dependent aggressive anion. As corrosion propagates, the acidity and aggressiveness of the crevice solution increases as a result of metal dissolution and hydrolysis, creating an autocatalytic electrochemical cell.

Species-dependent crevice corrosion applications include fastener assemblies submerged in seawater for naval applications, atmospheric fastener assemblies for automotive and aircraft applications, coating delamination, and porous electrolyte deposits, for example. Nickel alloys are widely used in applications because they are corrosion resistant alloys that are suitable for most corrosive environments. Without crevices and local acidification, the oxide layer on nickel alloys is extremely stable and uniform corrosion rates remain sufficiently low. However, corrosion

Submitted for publication: February 27, 2016. Revised and accepted: May 31, 2016. Preprint available online: May 31, 2016, http://dx.doi.org/10.5006/2065.

‡ Corresponding author. E-mail: gyoung1@uakron.edu.
* Department of Mathematics, The University of Akron, Akron, OH 44325-4002.
** Department of Biomolecular and Chemical Engineering, The University of Akron, Akron, OH 44325-4002.

ISSN 0010-9312 (print), 1938-159X (online)
16/000199/$5.00+$0.50/0

resistant alloys are susceptible to severe crevice corrosion in extremely thin/long crevice domains.[1-2]

Ni-625 (UNS N06625[(1)]) crevice corrosion has been characterized through three underlying stages.[1,3-5] Stage 1 is the time prior to induction and contains deoxygenation, separation of anode/cathode, and ennoblement of the exterior cathodic surface. Stage 2 is the induction period and accounts for a local initiation site and transport processes within the crevice that result in increasing crevice solution aggressiveness and acidification. Stage 3 is the aggressive propagation of the interior anodic crevice that is driven by IR drop and the shape of the potentiodynamic polarization curve in the critical crevice solution. This stage continues until metal oxide repassivation or material failure.

Considering experimental efforts to investigate crevice corrosion, Dejong[6] and Lee, et al.,[7] stated that the difficulty with obtaining quantitative understanding of crevice corrosion has been the inability to measure key features within the crevice, such as spatially-dependent species concentrations.[8-11] Hence, electrochemical tests are used to predict the corrosion behavior in simulated critical crevice solutions (CCS). Regarding Ni-625, Jakupi, et al.,[12] determined that the rate of oxygen reduction on the exterior surface is the limiting parameter for repassivation vs. stable propagation. Only in cases where the polarization potential exterior to the crevice reached and remained at E = 0.20 V did crevice corrosion propagation stabilize. Martin, et al.,[13] and Shaw, et al.,[14] demonstrate a self-ennobling mechanism for Ni-625 crevice corrosion initiation. Through the first few days, the initial potential vs. SCE is between –0.20 V and –0.30 V. Through 50 d of bulk ocean water immersion, the potential increases between 0.40 V and 0.50 V. After potential ennoblement, crevice corrosion may initiate and propagate if the cathodic reduction remains sufficient. Martin, et al.,[15] generated damage evolution experiments for Ni-625 assemblies with polarized bulk exterior surfaces at 65°C. However, there is still a lack of experimental damage history profiles.

The majority of published galvanic and crevice corrosion models are well-mixed and stationary in time. Well-mixed modeling research is applicable for large crevice gaps with forced convection, where the interior crevice species and pH are uniform and match the bulk concentrations. The magnitude of the conductivity of the electrolyte κ, the magnitude of the current density i(E), and the domain geometry (L is the length of the crevice, w is the crevice gap width, and d is the depth in the additional Cartesian dimension of the crevice) control the amount of IR drop down the length of the crevice and the rate of dissolution.[16-17] An equation estimating this IR drop (ΔE) relationship is:

$$\Delta E = [I][R] = [i(E)Ld]\left[\frac{L}{\kappa wd}\right] \quad (1)$$

For concentration-dependent IR drops, the equivalent conductivity is a function of the spatially-dependent species concentrations, C_i, and the assumed spatially constant diffusion coefficients, D_i:

$$\kappa(C_i) = \frac{F_a^2}{R_g T}\sum_i Z_i^2 D_i C_i \quad (2)$$

where F_a is Faraday's constant, R_g is the gas constant, T is temperature, and Z_i are valences.

There are two separate, but complimentary, modeling approaches to simulate crevice corrosion: (i) initiation modeling and (ii) propagation modeling. Initiation modeling requires mass transfer time-dependent analyses that are more easily solved for constant passive currents, and account for the time of deoxygenation and development of the CCS. Propagation modeling often assumes steady state mass transport and only considers a time scale for the rate of the corroding electrode (i.e., mass transport is much faster than dissolution).

The foundation of species-dependent crevice corrosion initiation modeling was developed by Turnbull,[18-19] Sharland,[20-22] and Walton.[23-25] Walton, et al.,[24-25] explored the possibility of solving the full 1D Sharland system using finite element methods, and introduced a single polarization curve that is representative of the electrode surface reaction in a bulk electrolyte solution. For nickel alloys, however, it is not feasible that the bulk anodic polarization curve properly describes the surface reaction inside the crevice after initiation. Thus, a model is needed to allow for the time-dependent initiation of crevice corrosion followed by the long-term propagation, via the CCS. Engelhardt, et al.,[26] proposed a numerical initial time crevice corrosion model that incorporates surface and bulk reactions. The results predict potential and species distributions for six ionic species and O_2, but are only presented for constant passive current density fluxes and equilibrium reactions.

Kelly and Stewart,[27] on the other hand, replaced the constant current density assumption with polarization behavior characterized by an assumed set of pH-dependent polarization curves. These curves described a hypothesized stainless steel that did not exhibit active/passive behavior in the occluded region of the crevice. This is in contrast to the Ni-625 crevices in seawater investigated here. Further contrasts between the Kelly and Stewart[27] investigation and the present work are in the high applied polarization used external to the crevice in the present work, and inclusion of modeling of the free boundary for damage evolution. Nevertheless, both the present work and Kelly and Stewart[27] include the combination of IR drop with CCS.

(1) UNS numbers are listed in *Metals and Alloys in the Unified Numbering System*, published by the Society of Automotive Engineers (SAE International) and cosponsored by ASTM International.

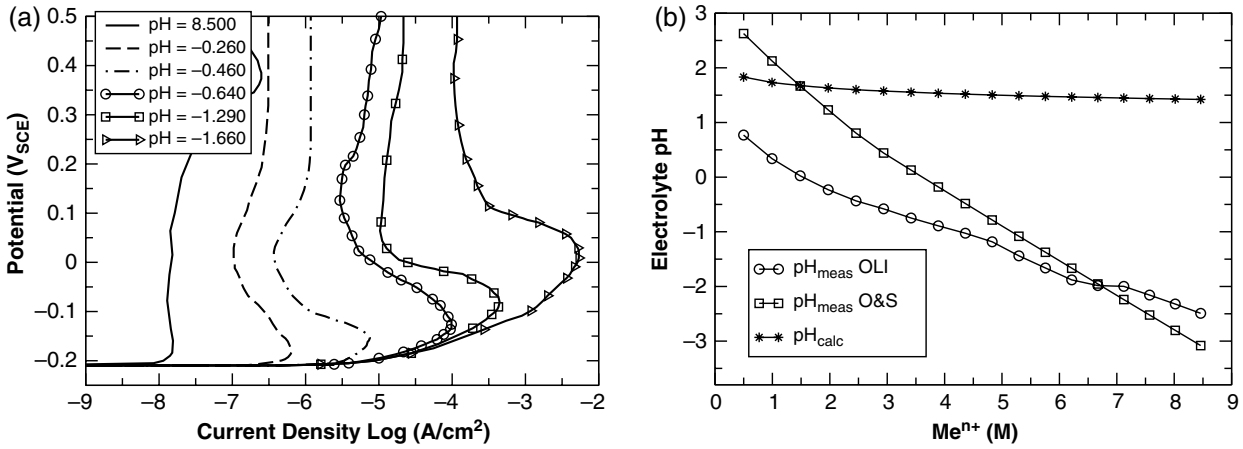

FIGURE 1. *(a) pH-dependent anodic polarization curves for Ni-625 in HCl solution[1] and a bulk anodic curve in artificial seawater.[14] (b) pH and Me^{n+} relationships.[4,29]*

The work presented here fills in some of the experimental gaps through measurement of damage evolution profiles for Ni-625 crevices in seawater. This work also extends modeling efforts by utilizing species-dependent experimental data to calculate the time-dependent corrosion evolution, and spatially-dependent species and potential distributions in extremely tight crevice gaps. The coordinated experimental and modeling efforts assist in defining the experiments that need to be conducted to improve model input and provide validation data, give insight into corrosion mechanisms, define a general modeling approach for application to additional material systems, and provide insight for incorporating the modeling approach into advanced commercially available software packages.

EXPERIMENTAL EFFORTS AND RESULTS

The mathematical model for Ni-625, developed below, requires several empirical inputs. Species-dependent polarization curves are needed to quantify the effects of surface reactions. pH vs. Ni-625 alloy composition relationships are required to quantify bulk hydrolysis chemical reactions and hydroxide precipitation reactions. Further, measured damage evolution profiles are used to validate the stages of initiation and propagation of aggressive dissolution, and to provide benchmarks for model calculations of the damage. The experimental efforts to obtain the needed data are outlined next.[28]

Experimental Input Data

The polarization curves for Ni-625 are used in a simulated HCl solution (Figure 1[a]), obtained in Lillard, et al.[1] Here, the pH is the experimentally measured pH. In these highly concentrated hydrogen solutions, the pH is dependent on the Cl^- concentration, C_{HCl}. Lillard, et al.,[1] use the expression:

$$pH = -\log(\gamma_{HCl} C_{HCl}) = -1.53 I_S - \log_{10}(C_{HCl}) \quad (3)$$

where $I_S = 0.5 \sum C_i Z_i^2$ is the ionic strength of the HCl electrolyte solution that is equal to the concentration of HCl for this 1:1 electrolyte, and γ is the activity to determine the pH.

The polarization curves provide electrochemical responses as a function of measured pH, referred to as pH_{meas}, while the mathematical model calculates pH, referred to as pH_{calc}, based upon H^+ concentration. Thus, pH_{calc} values must be converted to measured values in order to use the polarization curves. Furthermore, the model accounts for hydrolysis and hydroxide precipitation reactions by assuming an equilibrium relationship between pH_{calc} and the metal ion concentration Me^{n+}. Hence, two relationships, one between pH_{meas} and pH_{calc}, and one between pH_{calc} and Me^{n+}, are needed. These relationships allow one to relate the experimental polarization curves to the hydrolysis and precipitation reactions and account for the severe acidification that is observed in experiments.

To define these relationships, information from OLI software[†,29] and the work of Oldfield and Sutton (O&S)[4] were used, presented in Figure 1(b). In basic terms, one calculates the value of Me^{n+} (described later in this manuscript) and then reads off the corresponding value of pH_{meas} from Figure 1(b). This procedure is implemented as follows. Using the 18 data points from the pH_{calc} curve in Figure 1(b), the corresponding pH_{calc} and Me^{n+} relationship is derived:

$$pH_{calc} = 1.53 - 1/3 \log[CrCl_3] \quad (4)$$

where $CrCl_3 = 0.2477\ Me^{n+}$ M. To get the relationship between pH_{meas} and pH_{calc}, the O&S[4] relationships are used:

$$pH_{meas} = pH_{calc} + 0.6(2.0 - [CrCl_3]) - 0.23([FeCl_2] + [NiCl_2] + [MoCl_3]) \quad (5)$$

[†] Trade name.

for $CrCl_3 \leq 2.0$ N, and

$$pH_{meas} = pH_{calc} - 0.33([CrCl_3] - 2.0) - 0.23([FeCl_2] + [NiCl_2] + [MoCl_3]) \quad (6)$$

for $CrCl_3 > 2.0$ N. The concentrations $NiCl_2$, $CrCl_3$, $MoCl_3$, $FeCl_2$, and $NbCl_3$ in Equations (5) and (6) are in normality, where normality is the product of molarity and valence. The concentration $CrCl_3$ in the pH_{calc} expression is in molarity. Using Equations (4) through (6), there is now a relationship between pH_{meas} and Me^{n+}. Note that this relationship and the software-computed relationship[29] shown in Figure 1(b) are similar for Me^{n+} values above 5.0 M. It will be shown that the CCS exists in this region of high metal concentration.

In summary, Equation (4) and equilibrium expressions define the hydrolysis and precipitation reactions in the mathematical model. The six polarization curves in Figure 1(a), each identified by a specific pH_{meas} value, correspond to the pH_{calc} and Me^{n+} sets:

$$pH_{calc} = [8.500, 1.531, 1.520, 1.511, 1.482, 1.468] \quad (7)$$

and

$$Me^{n+} = [0.000, 4.014, 4.324, 4.604, 5.622, 6.204] \text{ M} \quad (8)$$

From here, interpolation can be used to calculate additional polarization curves, as needed by the model.

Experimental Potentiostatic Damage Evolution

Measurements from damage evolution experiments for a Ni-625 fastener assembly are used for validation of the model. The experiments were repeated multiple times to ensure reproducibility. Further, there was little variability in results from one experimental run to another. A schematic of the experimental setup (with unknown gap thickness and a torque of 5 ft·lb [6.78 N·m]) is shown in Figure 2. The electrolyte is artificial seawater, the crevice length is x = 1.27 cm, and the electrochemical cell (fastener assembly) is polarized at E = 0.20 V to ensure accelerated initiation times. After the potentiostatic hold, the test specimen is removed from the electrolyte, disassembled, cleaned of any corrosion products, and analyzed for corrosion damage.

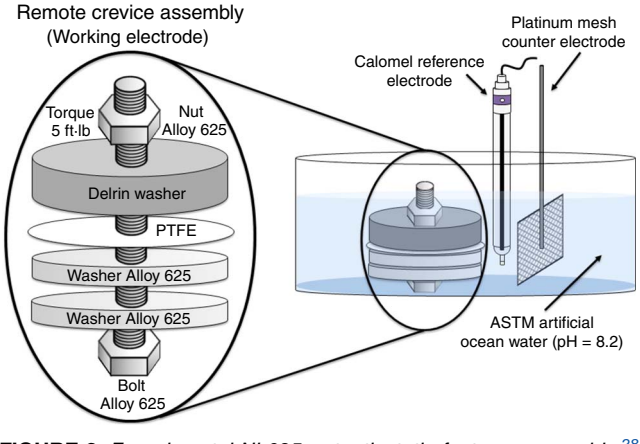

FIGURE 2. *Experimental Ni-625 potentiostatic fastener assembly.*[28]

The surface profiles after metal dissolution, for the potentiostatic holds, are shown in Figure 3 through 72.0 h. In these experiments, crevice corrosion was always observed to be initiated at the tip of the crevice (1.27 cm) and to progress toward the mouth (0.0 cm). From a planar view, this progression left many "beach-line" marks on the surface of the creviced area that overlapped one another. Presumably this owed to multiple critical crevice solutions of varying concentration (and thus corrosion rates) radiating outward from the initiation sites at the tip. In cross section, the intersection of these beach marks appears as secondary sites of attack (double dips in the damage profile). However, these are not multiple initiation points.

At 10.0 h, it is shown that the initiation process has begun and some small dissolution has taken place near the crevice tip. At the 24.0 h time history, it was noticed that this cell of dissolution moved toward the crevice mouth. However, damage does not continue behind the cell (leading to a uniformly damaged crevice). From approximately 48.0 h onward, the damage does not progress any closer to the crevice mouth and rapid propagation ensues. This is consistent with a process that is controlled by IR drop and the shape of the polarization curve in the critical crevice solution. Specifically, a location of 0.2 cm to 0.3 cm is likely the location of IR* for this crevice geometry (gap) and the oxidation rate is occurring at the maximum in the active to passive peak in the polarization curve.

Test specimens that were removed after initiation of aggressive propagation developed severe precipitation accumulation at the crevice mouth (both interior and exterior to the crevice mouth). This observation implies that the entire crevice electrolyte has reached the CCS saturation limit, and that there is a severely sharp concentration boundary layer that occurs near the crevice mouth. This leads to model scenarios with concentration gradients at the mouth, and that are nearly well-mixed at the CCS near the tip.

The damage results are not uniform over space and time, and show peak damage rates of approximately 1.5 μm/12.0 h in the induction stage and 12.0 μm/12.0 h in the propagation stage. Specifically, these rates are calculated from the damage profiles and, therefore, provide an average rate throughout the time of damage shown. From Faraday's law, these rates correspond to a limiting active current density of 1.0×10^{-4} A/cm^2 and an active peak current density of 8.0×10^{-4} A/cm^2. Because the damage is not uniform over space, these rates are calculated from the damage profiles and, therefore, provide an average rate throughout the time of damage shown. The limiting

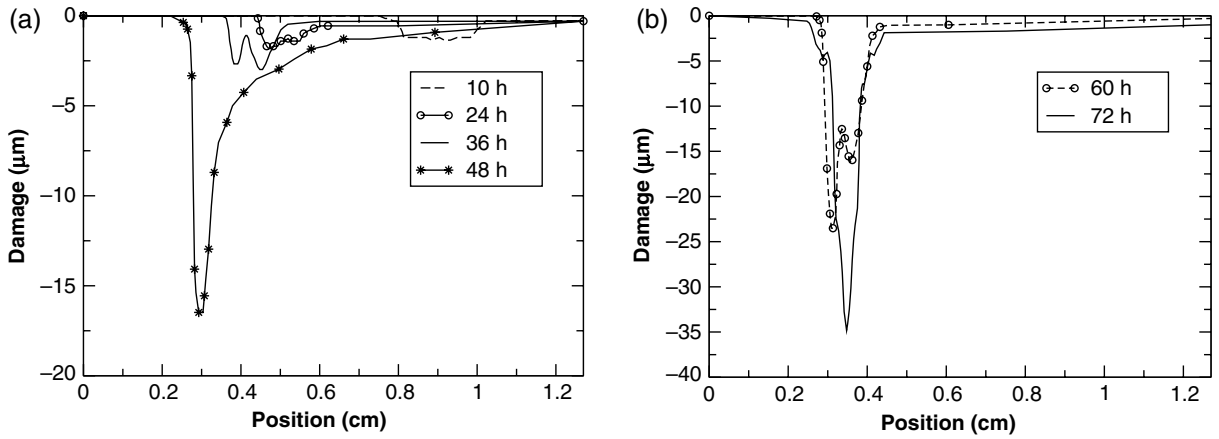

FIGURE 3. *(a) Snapshots of the Ni-625 internal fastener assembly (torque = 5 ft·lb [6.78 N·m]) damage through 48 h of submersion and polarization at 0.20 V, and (b) snapshots at 60 h and 72 h for the same conditions.[28] 0.0 cm denotes the location of the crevice mouth, while 1.27 cm denotes the crevice tip.*

current density is used to define the rate of the propagating CCS cell in the Stage 2 model discussed in the next section. The active current density is the peak rate of dissolution in the Stage 3 model, and is slightly above the peak anodic current density of the 5th, $pH_{meas} = -1.290$, polarization curve in Figure 1(a). Hence, the faster rate was used to provide guidance for obtaining the final interpolated polarization curve used in the Stage 3 model.

The total current response from the potentiostatic experiment, shown in Figure 4(a), is examined to define mechanistic trends. Further, the total anodic current that is calculated from the damage profiles in Figure 3 is shown in Figure 4(b).[28] For this calculation, the velocity of the damage front was approximated using the curves in Figure 3. Then the current density was calculated using Faraday's law (Equation [15]). Next, the damage profiles (defining the interface velocity) were integrated down the length of the crevice, assuming the third dimension in and out of Figure 3 was 1.0 cm (to integrate current density over the total surface area). From the experimental results, it was observed that the corrosion that initiated near the crevice tip occurred at some time between 5.0 h and 10.0 h per sample. Thus, 10.0 h was taken as the initial time in the velocity calculation from the damage profiles. The total currents, calculated in this fashion, were considered conservative values as they are calculated from an approximate instantaneous current density function. The trends of the experimental and calculated potentiostatic total currents were consistent, and demonstrated three stages of the corrosion process.

MATHEMATICAL MODELING EFFORTS AND RESULTS

Results for two 1D thin-film crevice configurations are presented. The first, Figure 5(a), is representative of an atmospheric crevice with a nonconstant,

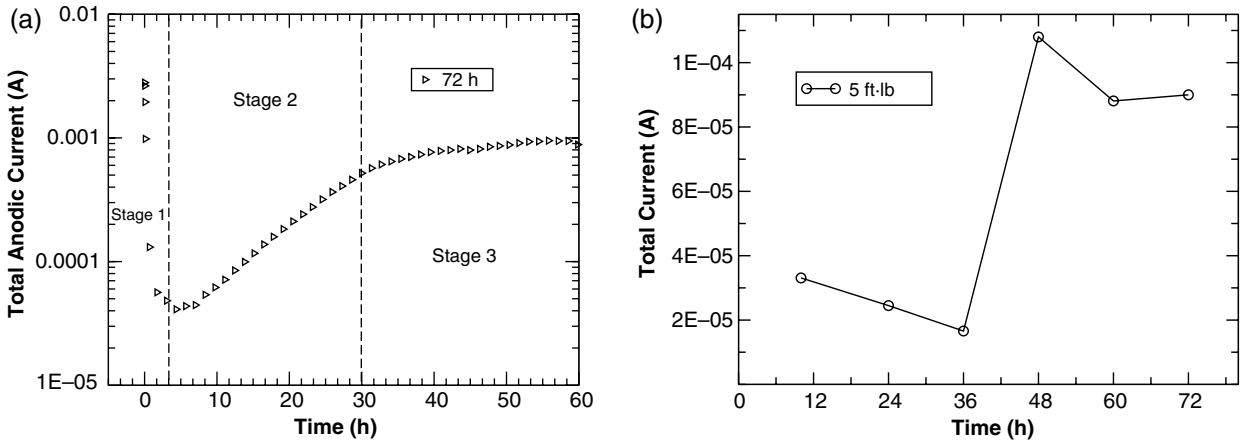

FIGURE 4. *(a) Experimentally measured total anodic current for the entire Ni-625 fastener assembly interior and exterior to the crevice, and (b) total anodic current inside of the crevice calculated from the time-dependent damage profiles in Figure 3 using Faraday's law.*

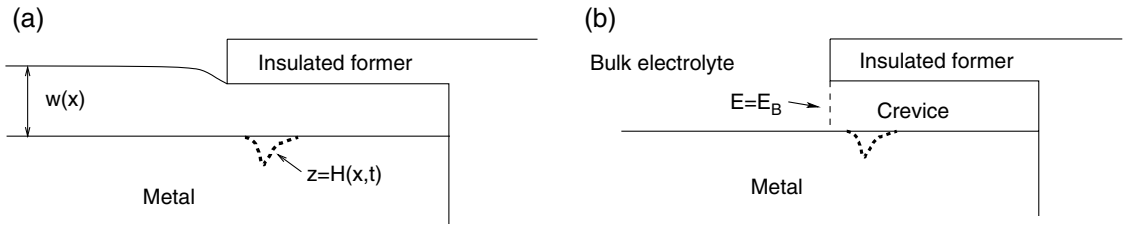

FIGURE 5. *(a) Thin-film, interior and exterior, crevice electrolyte domain with a prescribed, nonconstant electrolyte thickness w(x) (atmospheric crevice corrosion). The x direction is along the metal substrate, with the origin at the crevice mouth. (b) Thin-film, interior, crevice electrolyte domain adjacent to a bulk 2D electrolyte, where the mouth potential is equal to the polarized bulk electrode surface potential E_B. The dotted line, z = H(x,t), denotes the time-dependent damaged location of the metal/electrolyte interface resulting from corrosion.*

thin-film interior/exterior crevice electrolyte thickness.[26] The well-mixed studies[17,30] show that increasing the electrolyte thickness decreases the IR drop (Equation [1]). Thus, it is important to model the 1D thin-film limitation for the bulk electrolyte thickness. If the electrolyte thickness increases beyond the 1D limit, then a well-mixed bulk electrolyte is assumed. The bulk exterior/thin-film interior configuration is shown in Figure 5(b) and is representative of submerged crevice assemblies. Here it is assumed that the boldly exposed metal surface is experimentally polarized to a given potential. For the Ni-625 application, with adjacent bulk electrode surface polarized and thin crevice gap, there is minimal IR drop between the polarized surface and the crevice mouth. Hence, the potential at the crevice mouth is specified. A no-flux condition is imposed at the crevice tip, and the species-dependent system is only solved in the interior crevice electrolyte.

Various 1D systems will be examined, as stepping-stones, leading up to the final Ni-625 propagation model. The final model will combine knowledge gained from the introductory models, demonstrate agreement with the experimental Ni-625 crevice corrosion results, and provide scientific understanding into crevice corrosion mechanisms of Ni-625.

Stage 1 Deoxygenation and Stage 2 Development of the Critical Crevice Solutions

During initiation of crevice corrosion, two diffusion-dominated mechanisms (deoxygenation [Stage 1] and metal ion dissolution building up to the CCS [Stage 2]) are examined. The Stage 1 model is:

$$\frac{\partial O_2}{\partial t} = D_O \frac{\partial^2 O_2}{\partial x^2} - \frac{i_c}{4wF_a}\left(\frac{O_2}{O_{2bulk}}\right) \tag{9}$$

$$\text{s.t. } O_2(x=0) = O_{2bulk},\ \frac{\partial O_2(x=1.27)}{\partial x} = 0 \text{ and } O_2(t=0) = O_{2bulk} \tag{10}$$

Solving this numerically (finite differences) determines the time and location of oxygen depletion within the crevice, as well as provides a predicted crevice gap for the fastener experiment described earlier. The transient oxygen concentration distributions for two variations of crevice gap and an anodic passive current of $i_c = 2.4 \times 10^{-8}$ A/cm^2 are shown in Figure 6. The final concentration profiles demonstrate the time that oxygen diffusion reaches steady state. Crevice depths that yield oxygen concentrations less than 1/5 of the bulk concentration are considered oxygen

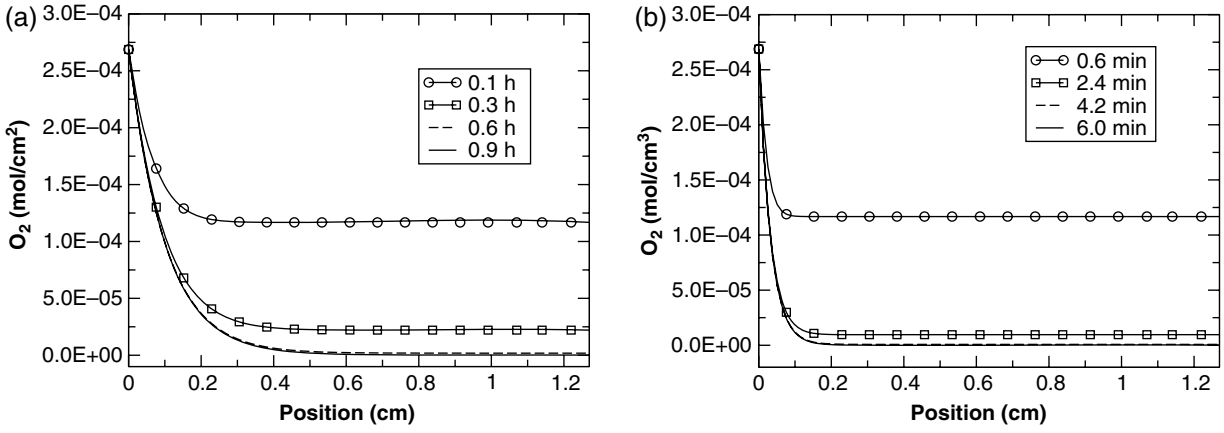

FIGURE 6. *(a) Time-dependent depletion of oxygen inside the crevice for w = 1.0 μm, O_{2bulk} = 8.6 ppm, and $i_c = 2.4 \times 10^{-8}$ A/cm^2 and (b) time-dependent depletion of oxygen inside the crevice for w = 0.1 μm.*

depleted. Based upon the location of maximum damage in the fastener experiments (0.20 cm ≤ x ≤ 0.40 cm) and the time until the start of the induction stage, the time-dependent solutions suggest that the fastener crevice gap must be of the order of w ≤ 1.0 μm to ensure deoxygenation.

After deoxygenation of the crevice, the anodic oxidation reaction (at the passive current density) occurs on the entire electrode surface inside the crevice and the cathodic oxygen reduction reaction occurs on the entire boldly exposed metal surface that is exterior to the crevice. It is assumed that at some instance in time an event occurs that breaks down the passive layer and allows for active dissolution of the metal surface. At this location (assumed here to be at the crevice tip based upon the experimental early time damage profiles), there is a spike in current and a localized critical crevice solution is created. This cell of metal ionic species then diffuses throughout the crevice, increasing the amount of metal dissolution, increasing the total current, and saturating the solution at the critical crevice solution. This stage is complete when crevice corrosion initiation occurs with permanent passivity breakdown. Thus, the Me^{n+} diffusion model for Stage 2 is:

$$\frac{\partial Me^{n+}}{\partial t} = D_M \frac{\partial^2 Me^{n+}}{\partial x^2} + \frac{i_a}{nwF_a} \tag{11}$$

$$\text{s.t. } M(x=0) = M_{mouth},\ M(x=1.27) = M_{CCS},\ \text{and}\ M(t=0) = M_{bulk} \tag{12}$$

Here, it is assumed that a concentration spike of M_{CCS} instantaneously occurs at the cell represented by crevice tip to initiate the stage. The value of M_{CCS} is determined to be 5.6 M, using software.[29] At metal concentrations above 5.6 M, dissolution is characterized by precipitation of $NiCl_2$. Therefore, this concentration represents the upper bound as there is evidence that stable corrosion has been seen to progress at surface concentrations more dilute than those resulting in a salt film.[31] This cell of critical crevice solution then diffuses throughout the crevice electrolyte. The time for the entire crevice solution to reach saturation is the time of crevice corrosion initiation. Beyond this time, it is assumed that there is passive layer breakdown and aggressive dissolution continually propagates (Stage 3). From the experimental potentiostatic total current measurements and damage profiles, Stage 2 occurs between 5.0 h and 36.0 h, and leads to a relatively uniform damage profile. To capture these effects in the time-dependent 1D transport analysis, the anodic surface reaction term, with i_a in Equation (11), is prescribed as a piecewise current (Figure 7[a]) to simulate the corrosive cell structure.

The calculated transient Me^{n+} concentration distributions are shown in Figure 7(b). The final concentration profiles demonstrate the time for metal ion concentrations to reach steady state. The results show that a crevice gap of less than w = 1.0 μm is required for saturation at the CCS when $i_a = 2.4 \times 10^{-8}$ A/cm^2. The time to reach metal ion saturation in this case is 18.0 h, consistent with the experiments. For all cases, the time to reach and depth of the CCS are both increased with a decrease in the M_{mouth} concentration and anodic passive current density.

This metal ion diffusion simulation is a suggested mechanism for the Stage 2 initiation that appears to be appropriate for the current experimental results. From this model, one is able to validate the time of initiation, give insight into the concentration distribution of Me^{n+}, demonstrate feasible ranges of crevice gap and anodic current, and provide an initial

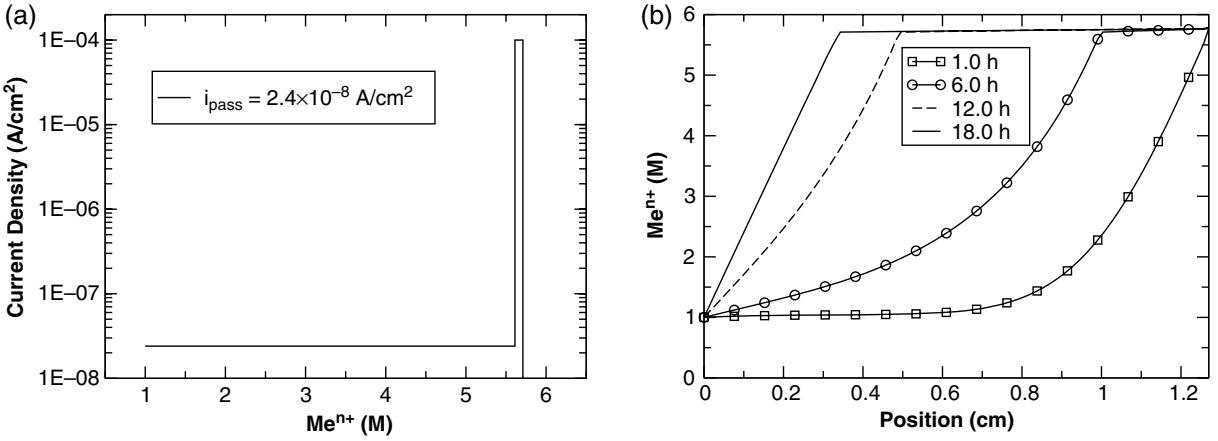

FIGURE 7. *(a) Piecewise anodic current density function that is the passive bulk current of $i_a = 2.4 \times 10^{-8}$ A/cm^2 for 0 ≤ Me^{n+} ≤ 5.611 M, the active current of $i_a = 1.0 \times 10^{-4}$ A/cm^2 for 5.611 ≤ Me^{n+} ≤ 5.711 M, and zero current for Me^{n+} > 5.711 M, and (b) transient Me^{n+} distribution for w = 1.0 μm, M_{mouth} = 4.6 M, and $i_a = 2.4 \times 10^{-8}$ A/cm^2.*

concentration condition for the long-term, Stage 3 simulation that follows.

Stage 3 Corrosion Propagation

Using a thin-film approximation, $w \ll L$, the governing system of equations is reduced from 2D to 1D for steady-state mass transfer applications. The reduction of order technique integrates through the vertical direction of the electrolyte and incorporates the top and bottom flux boundary conditions into the governing equations. After initiation of crevice corrosion (saturation of the crevice electrolyte composition at CCS) it is generally accepted that mass transfer has reached steady state compared to the time of corrosion damage evolution. The resulting governing system of 1D transport equations is:

$$\frac{\partial}{\partial x}\left[\left(-D_i\frac{\partial C_i}{\partial x}+\frac{Z_i F_a D_i}{R_g T}C_i\frac{\partial E}{\partial x}\right)(w+H)\right] = r_i + R_i(w+H) \quad \text{and} \quad \sum_i Z_i C_i = 0 \tag{13}$$

$$\text{s.t. } \bar{J}_i\cdot\hat{n} = 0 \text{ at } x = -LC, LA \tag{14}$$

where $\bar{J}_i\cdot\hat{n}$ is the flux in the direction of the unit outward normal vector, LA is the crevice tip location, –LC is the far-field exterior crevice electrolyte boundary location, and H(x, t) is a functional shape of the corroded electrode surface. Here, r_i denotes the surface reactions, incorporated through the current densities obtained from the polarization curves. R_i denotes the bulk chemical reactions that are discussed below. An electroneutrality condition is also imposed.

To model the time-dependent damage evolution in the 1D system, the metal/electrolyte interface location is defined, z = H(x, t), and the damage equation is determined from Faraday's law:

$$\frac{H_t}{\sqrt{1+(H_x)^2}} = \frac{i_a(E, pH_{calc}, Me^{n+})E_W}{F_a\rho} \tag{15}$$

Here, E_w is the molecular weight and ρ is the alloy density. The initial condition is H(x, 0) = 0. The interface, z = H(x, t), restricts the shape of this front to be the graph of a function of x. Hence, corrosion leading to damage that undercuts the metal is not accounted for in the 1D formulation. The fully coupled 1D system of equations is numerically difficult to solve. Using algebraic manipulation, similar to that of Sharland,[21] the system can be rotated and rewritten as a boundary value problem (BVP) for just two unknowns, Me^{n+} and E. In this process, the bulk reactions, R_i, are all determined in terms of Me^{n+} using equilibrium expressions and Equation (4).

The 1D, BVP rotated system of equations has the generic form:

$$Me^{n+}_{xx} = F(Me^{n+}, Me^{n+}_x, E, E_x) \tag{16}$$

$$E_{xx} = G(Me^{n+}, Me^{n+}_x, E, E_x) \tag{17}$$

$$\text{s.t. } J_M = 0 \text{ at } x = LA,\ Me^{n+} = Me^{n+}_{mouth} \quad \text{and} \quad E = E_{mouth} \text{ at } x = 0 \tag{18}$$

Here, the terms on the right hand side are nonlinear functions of Me^{n+} and E. This system of equations is solved using the Matlab† routine *bvp5c*. All details may be found in Stenta.[32]

To validate the BVP solution, analytical solutions to Equations (16) through (18) are determined in the limit of a two species (Me^{n+} and Cl^-) system with no reactions, no damage, and a constant current source:

$$Me^{n+} = -\frac{i_a(x^2/2 - LAx)}{wnF_aD_M(1+n)} + Me^{n+}_{mouth} \tag{19}$$

$$E = -\frac{1}{\alpha}\ln\left(-\frac{i_a(x^2/2 - LAx)e^{-\alpha E_{mouth}}}{wnF_aD_M(1+n)M_{mouth}} + e^{-\alpha E_{mouth}}\right) \quad \text{for } \alpha = \frac{F_a}{R_g T} \tag{20}$$

A solution to a three-species system is derived in a similar fashion.[32] For all of these situations the 1D BVP solutions match the analytical solutions. Likewise, 1D/2D COMSOL† solutions match exactly.

Next the chemical equilibrium conditions for hydrolysis, hydroxide precipitation, and dissociation of water[26] are included into the simplified system. Including additional ionic species requires the solution of a larger system of equations with more unknowns. Under the equilibrium assumption, algebraic relationships are derived for all secondary species as a function of the metal ion. The BVP system for Me^{n+} and E is solved alone, and the remaining unknowns are back-calculated (all species are incorporated into the governing system through their equilibrium expression, but are solved for using Me^{n+}).[32] Note that for this setup Engelhardt, et al.,[26] investigate an interior/exterior species-dependent system for a similar alloy (Nickel C-22†) and an atmospheric application.

The interior/exterior domain configuration is shown in Figure 5(a). The calculated potential distribution is shown in Figure 8, for increasing variations in the exterior electrolyte thickness, to determine the effect of cathodic IR on the interior crevice. It was noticed that as w_{ext} increased, the IR in the bulk decreased and the IR in the crevice increased. Pushing the limits of the 1D approximation to w_{ext} = 1.0 cm, the thin-film limit is exceeded and reverts to the bulk electrolyte configuration (Figure 5[b]).

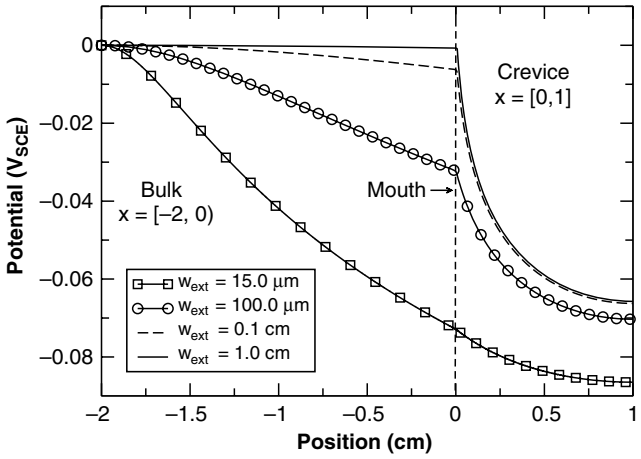

FIGURE 8. *Parameter study of the IR drop for various w_{ext} and w_{int} = 10 μm.*

The calculated species concentrations are presented in Figure 9 for several exterior film thicknesses. The species concentrations demonstrate large gradients inside the crevice and nearly zero gradients outside the crevice for large bulk electrolyte thicknesses exceeding w_{ext} = 1.0 cm. A key feature that is not observed in the species concentrations is a large H^+ gradient leading to an acidic pH at the crevice tip. This is a requirement for Ni-625 crevice corrosion initiation.

Hence, species-dependent polarization curves and extreme acidification to predict species-dependent damage evolution in the Ni-625 system are incorporated. For this case, the species-dependent system is solved interior to the crevice only (Figure 5[b]) and cathodic reactions are not considered. The surface reaction along the electrode/electrolyte interface, inside the crevice, is anodic dissolution. The bulk reactions in the crevice electrolyte solution are hydrolysis, hydroxide precipitation, dissociation of water, and metal chloride precipitation. Dissociation and metal chloride precipitation are assumed in equilibrium, while the hydrolysis and hydroxide precipitation reactions are taken from experimental and theoretical relationships [Equations (4) through (6)] to allow for severe acidification.

To illustrate the use of the polarization curves in the solution procedure, refer to Figure 10. Here, from left to right, the first, second, and last curves are taken from Figure 1(a). As the pH varies along the length of the crevice with time, there are an infinite number of continuous interpolated path solutions through these curves to define the current density at the metal/electrolyte interface. Further, as Equations (16) through (18) are highly nonlinear, the numerical formulation needs an educated guess to guide it toward the appropriate interpolated path. This CCS guess curve, in Figure 10, is a polarization curve that has the same peak current density as the peak current density in the damage experiments. The remainder of the curve is linearly interpolated forward from the first and second curves.

The initial numerical simulations of the Stage 3 model calculated species profiles that corresponded to an equivalent conductivity for the electrolyte solutions (using Equation [2]) of κ = 2.088 S/cm. This is approximately eight times larger than the saturation limit of known NaCl and Cl^- solutions. Further, the calculated IR drop was such that the peak current density location, x_{crit}, is deep into the crevice and the spread of corrosion was far wider than experimentally observed. From this, refer to the literature and find that Walton[24] suggests a diffusion coefficient reduction is needed because the precipitation formation inside the crevice is slowing the rate of ionic species diffusion. Hence, the original diffusivity is reduced by a factor of 16, so the resulting conductivity is reasonable. Figures 11 and 12 show the resulting potential, current density, and damage profiles for $D_i^{new} = D_i^{old}/16$, where κ = 0.131 S/cm. All details may be found in Stenta.[32]

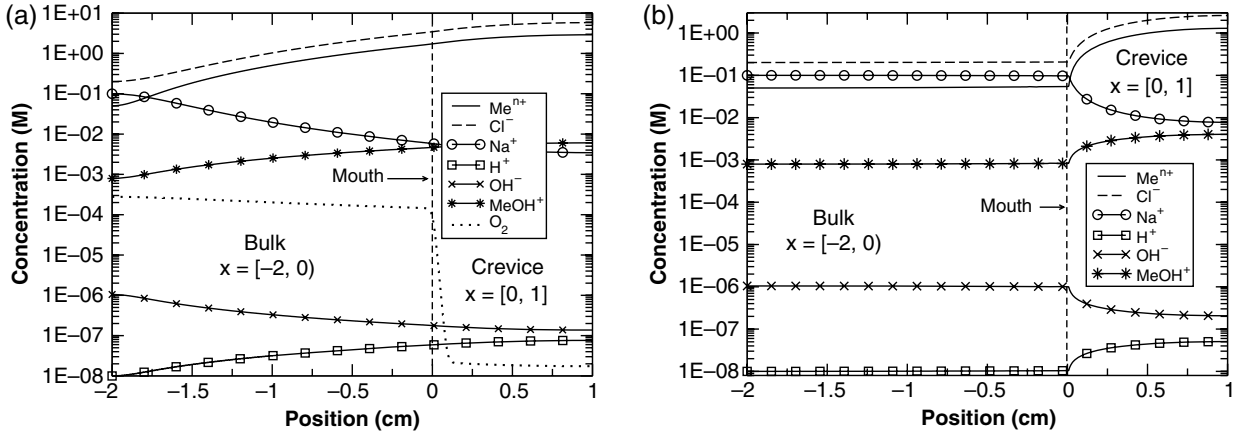

FIGURE 9. *(a) Interior/exterior six species system for validation of the Engelhardt, et al., data[26] with w_{int} = 10 μm, w_{ext} = 15 μm, and (b) species concentrations for the same parameters and w_{ext} = 1.0 cm.*

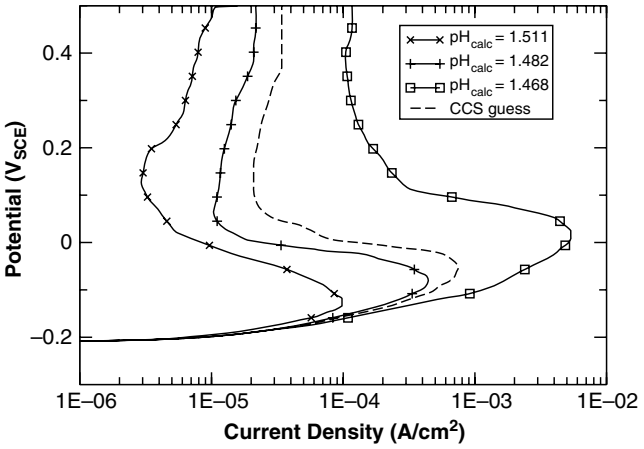

FIGURE 10. *Polarization curves that are used for the Stage 3 analysis.*

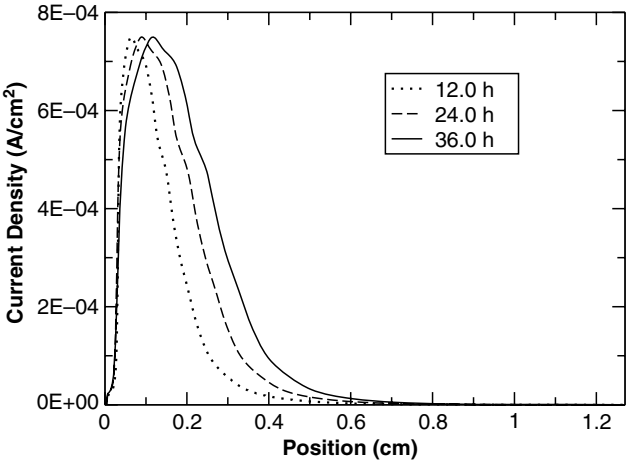

FIGURE 12. *Current density distribution through 36.0 h for w = 1.0 μm using the updated polarization curves and corrected diffusion coefficients (D_i/16).*

Next consider damage evolution results calculated from the well-mixed models.[16-17] These models require input of a single polarization curve and a conductivity. The final interpolated curve and equivalent conductivity that corresponds to the limiting concentration profiles from the species-dependent Stage 3 model calculations are used. Figure 13(a) shows that there is good agreement between the species-dependent and well-mixed damage evolution solutions. However, it would have been unlikely to solve the well-mixed problem without the knowledge of the species-dependent solution inputs: the appropriate equivalent conductivity, the limiting concentrations, the magnitude of the CCS, and the correct interpolated polarization curve. Given all of these, it is observed that the well-mixed solution agrees with the solution from the full species-dependent model. To explain this agreement, consider the concentration gradient near the mouth in Figure 7(b). In Stage 3, this concentration boundary layer narrows nearer to the mouth, and completely lies within the IR drop boundary layer (see the current density profile in Figure 12 to gauge the thickness of the IR drop boundary layer near the mouth). Hence, the well-mixed approximation reasonably approximates the full species case because the nonwell-mixed portion of the species system occurs in a crevice location that is prior to the location of the critical potential defining the passive to active peak in the polarization curve.

Figure 13(b) shows a comparison between the calculated damage evolution and the experimental damage evolution. The magnitudes of the calculated damage are in good agreement throughout the time history, as the appropriate polarization curve set is chosen for the CCS to match the peak current observed in the experimental Stage 3 damage profiles. Further, the total current in the D_i/16 case with the pH_{calc} = 1.468 polarization curve matches the experimental current. In addition, Figures 12 and 13 show that the current density and damage do vary spatially with time as the peak current density location changes as the gap width increases because of damage.

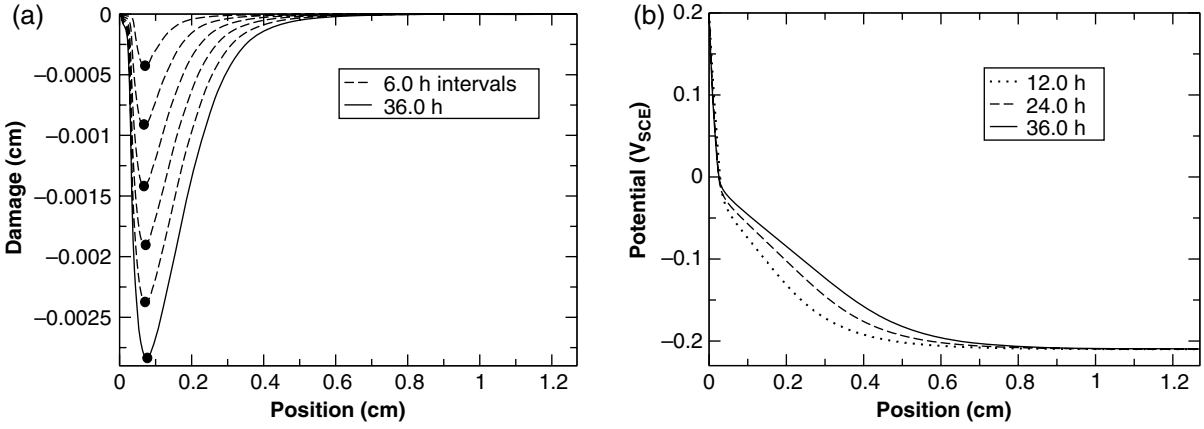

FIGURE 11. *(a) Damage through 36.0 h for w = 1.0 μm using corrected diffusion coefficients (D_i/16), and (b) potential through 36.0 h for w = 1.0 μm using the corrected diffusion coefficients (D_i/16).*

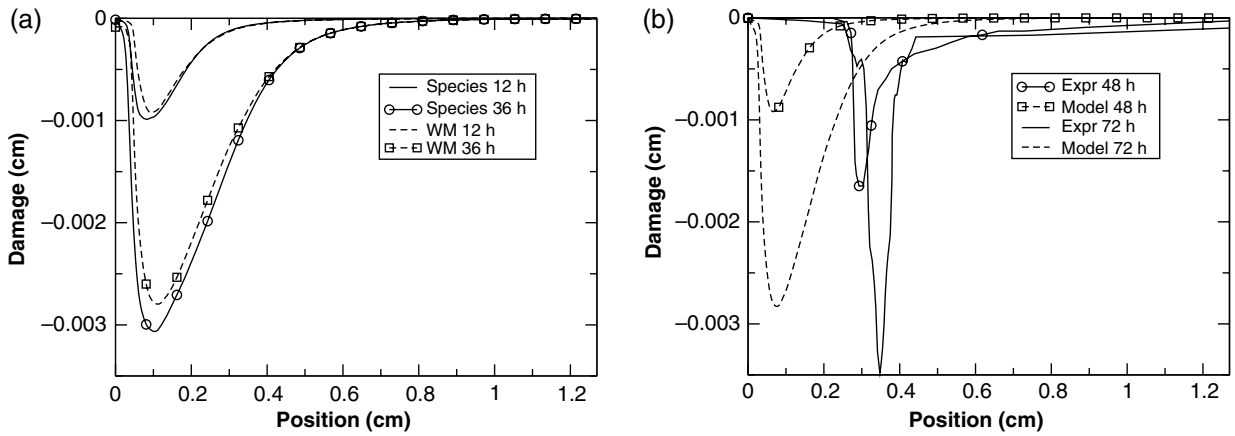

FIGURE 13. *(a) Species-dependent vs. well-mixed damage profiles through 36.0 h with w = 1.0 μm and $D_i/8$, and (b) overlaid $D_i/16$ model prediction with the experimental damage profiles through 72.0 h.*

However, the location of the damage within the crevice is inconsistent with experiments. The calculated location is much closer to the crevice mouth than the experimental observation. This occurs in the simulations because the metal concentration gradient is extremely sharp at the mouth. As a result, a large IR drop is immediately observed and damage accumulates near the mouth. However, this does not occur in the experiments. There is not a definitive explanation yet for why the experimental results show this wider passive zone near the mouth. Nevertheless, model calculations are used to examine two possible explanations.

First, there are several geometric differences between the model and the experiments. As shown in Figure 2, the experiments were conducted in a 3D, axisymmetric-type configuration, whereas the model is 2D. Further, the gap width in the model is established by two parallel and planar surfaces, so that the gap width is always constant down the length of the crevice. This idealized gap width is most likely not realized in the experiments (the actual gap width was not able to be measured in the experiments). Hence, the following modification to the model is posed: assume the gap width is wedge-shaped with wider width at the crevice mouth and narrower width at the tip. Figure 14(a) shows the calculated damage evolution using the wedge-shaped width (the width at the mouth is w = 10.0 μm and the width at the tip is w = 1.0 μm) and the experimental damage evolution, for the same model parameters as used in Figure 13(b). Per Equation (1), the wider gap width at the mouth leads to a smaller IR drop in this region of the crevice. Hence, a steeper IR drop occurs deeper within the crevice. This leads to the damage occurring deeper within the crevice and, as shown in Figure 14(a), somewhat better agreement between calculated and experimental peak damage locations. However, note that the wider gap width

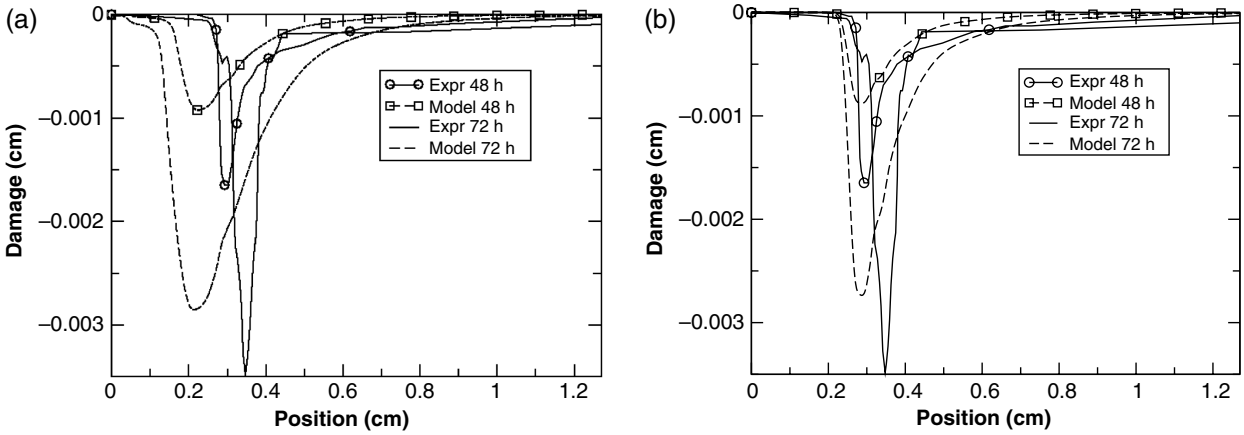

FIGURE 14. *(a) Comparison of calculated damage profiles with experimental damage profiles through 72.0 h using a wedge-shaped gap width (the width at the mouth is w = 10.0 μm and the width at the tip is w = 1.0 μm) in the model calculations, and (b) comparison of calculated damage profiles with experimental damage profiles through 72.0 h using the conjecture of an insulated region of width 0.25 cm and the wedge-shaped gap width at the crevice mouth in the model calculations.*

throughout the crevice length also leads to a widening of the damage profile resulting from the effect of the gap width on the potential profile.

A second scenario to explain the discrepancy between calculated and experimental damage evolution is the role of corrosion products. For example, such products may increase the electrolyte solution resistance through changes in the effective conductivity or gap width. Here, the focus is on their role in influencing the current distribution. It is assumed that the products are heavily accumulated near the crevice mouth (test specimens that were removed after initiation of aggressive propagation developed severe precipitation accumulation at the crevice mouth, both interior and exterior to the crevice mouth, despite the high acidification), and act as insulators to decrease the available electrode area.[33] To simulate this effect in the model, an insulated region of prescribed width at the crevice mouth is assumed. This is somewhat similar to calculations conducted by Stenta, et al.,[17] where an insulated region (along which no surface reactions and no damage occur) was placed between the cathode and anode in a galvanically coupled pipeline junction. Using such an insulated region (conjectured to begin at the crevice mouth and extend 0.25 cm into the crevice) and the wedge-shaped gap width described above in the model, Figure 14(b) shows the calculated damage evolution and the experimental damage evolution for the same model parameters as used in Figure 13(b). Together, the insulated region and the wider gap width at the mouth lead not only to a shallow linear drop in the potential near the mouth, but also a smaller active region that is reached deeper into the crevice. This leads to the damage occurring deeper and more localized within the crevice and, as shown in Figure 14(b), much better agreement between calculated and experimental peak damage locations. It is emphasized that the inclusion of the insulated region is a conjectured role for corrosion products, and that additional work is needed to modify the model to more properly account for the development and effects of these products.

Next, the location at which corrosion initiates within the crevice is examined using the original, constant gap width model. The initial x_{crit} location vs. crevice gap plots from several experimental investigations[1,4] and this study's results are shown in Figure 15(a). For large crevice gaps, the IR drop is not large enough to initiate crevice corrosion as the critical potential at the peak current density is not realized. Thus, a longer crevice is required to achieve sufficient IR drop. For extremely small crevice gaps, the IR drop is so large that all of the damage occurs just inside the crevice mouth. Here, the potential and current density gradients are too steep for the numerical simulations to capture.

The susceptibility to crevice corrosion initiation is demonstrated in Figure 15(b). Here, the shaded region shows feasible crevice configurations for initiation and the unshaded region defines configurations that are immune to crevice corrosion. Note that the experimental curves are more restrictive (for crevice gap), as they consider smaller currents for the critical crevice solution than those assumed here.

Finally, the authors comment on some issues with the numerical simulations. For nonconstant current density source functions, there is more than one steady state solution to the highly nonlinear system of equations. One solution is a nearly constant potential drop solution that is always stable. The other is a large IR drop solution relevant to corrosion. The constant potential solution corresponds to no corrosion and is initial condition dependent. It is always achieved if the initial condition is not near a large IR drop solution. The large IR solution becomes unstable when x_{crit} reaches the crevice tip. At this point, the only stable solution is the minimal IR drop solution, meaning that corrosion terminates. Further, appropriate system parameters must be chosen to permit a large IR drop for the first time step. For example, a short crevice length and/or a

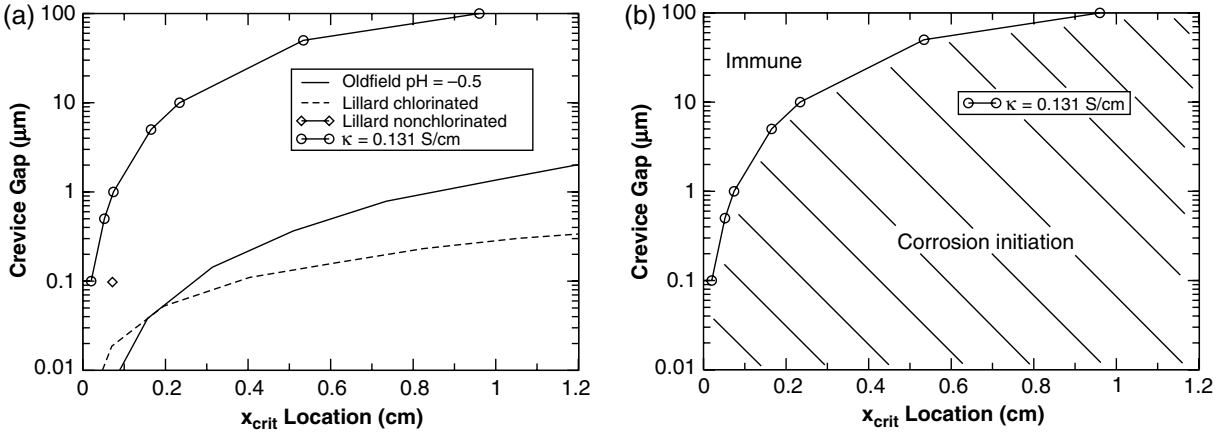

FIGURE 15. *(a) Initial corrosion time location of x_{crit} as a function of crevice gap, and (b) regions that are susceptible to crevice corrosion initiation for the D_i/16 simulation.*

large equivalent conductivity result in corrosion shut down and repassivation in a short time. This is a result of the total IR drop decreasing and x_{crit} moving toward the crevice tip.

SUMMARY AND CONCLUSIONS

In summary, the authors:

❖ Conducted corrosion experiments on Ni-625 fasteners and measured the time history of damage evolution and total current. These measurements indicated three stages in the corrosion process: deoxygenation, development of the critical crevice solution, and active crevice corrosion propagation. The experimental damage profiles indicated that slow corrosion began near the crevice tip and moved toward the mouth. Once the CCS was achieved, the corrosion rate drastically increased and damage was localized near the mouth.

❖ Developed a three-stage, 1D species-dependent transport model consistent with the experimental observations for Ni-625 crevice corrosion applications. Stage 1 is diffusion of oxygen out of the crevice, Stage 2 is diffusion of metal ion species throughout the crevice until the saturation of a critical crevice solution is obtained, and Stage 3 is the aggressive dissolution of the metal after the crevice has reached its CCS, and there is passive layer breakdown. The model incorporates species-dependent experimental input data for polarization curves that are a function of pH and metal ion concentration, theoretical pH and metal ion concentration data that define the equilibrium hydrolysis and hydroxide precipitation reactions, the CCS, and the limiting solubility concentrations.

❖ Developed analytical solutions to simplified species transport systems. These solutions are used for initial validation of the model compared to numerical results from 1D and 2D computer simulations. All simulations reproduce the analytical solutions.

❖ Developed numerical simulations of the full three-stage, nonlinear model. The calculated damage results are compared with experimental damage histories to demonstrate the ability of the model to capture known physical phenomena throughout the corrosion process, and to determine:

- The bounds for the experimentally unknown crevice gap,
- The minimal number of reactions that are required for modeling the damage evolution,
- Spatially- and time-dependent species concentration profiles down the length of the crevice throughout the various stages of the corrosion process, with corresponding potential and current density distributions.

❖ Demonstrated that a well-mixed solution model provides accurate results given appropriate input data for the polarization curve and equivalent conductivity that is determined from the solution of the species-dependent system.

❖ Modified the model to investigate the effects of hypothetical changes to the shape of the gap width, or a hypothetical decrease in the available electrode area resulting from the presence of corrosion products. Model calculations under both scenarios demonstrated that damage evolution occurs deeper within the crevice as observed in experiments. Such model modifications illustrate the capability of the model to account for general trends in how material and system parameters may influence the corrosion damage.

ACKNOWLEDGMENTS

This work is associated with the National Corrosion Center (NCERCAMP - National Center for Education and Research on Corrosion and Materials Performance) at The University of Akron and the DoD Technical Corrosion Collaboration supported by the U.S. Department of Defense Office of Corrosion Policy and Oversight through the U.S. Air Force Academy Grant FA7000-14-2-20016. The authors thank Daniel J. Dunmire and Richard Hays for their continued support.

REFERENCES

1. R.S. Lillard, M.P. Jurinski, J.R. Scully, *Corrosion* 50, 4 (1994): p. 251-265.
2. X. Shan, J.H. Payer, *J. Electrochem. Soc.* 156 (2009): p. C313-C321.
3. R.S. Lillard, J.R. Scully, *J. Electrochem. Soc.* 141, 11 (1994): p. 3006-3015.
4. J.W. Oldfield, W.H. Sutton, *Br. Corros. J.* 13, 1 (1978): p. 13-22.
5. J.W. Oldfield, W.H. Sutton, *Br. Corros. J.* 13 (1978): p. 104-111.
6. L.A. DeJong, "Investigations of Crevice Corrosion Scaling Laws Using Microfabrication Techniques and Modeling" (Master's thesis, University of Virginia, 1999).
7. J.S. Lee, M.L. Reed, R.G. Kelly, *J. Electrochem. Soc.* 151, 7 (2004): p. B423-B433.
8. M.I. Abdulsalam, H.W. Pickering, *Corros. Sci.* 41, 2 (1998): p. 351-372.
9. A.M. Al-Zahrani, H.W. Pickering, *Electrochim. Acta* 50 (2005): p. 3420-3435.
10. M. Vankeerberghen, *Corrosion* 60, 8 (2004): p. 707-717.
11. E. McCafferty, F.D. Bogar, E.D. Thomas, C.A. Creegan, K.E. Lucas, A.I. Kaznoff, *Corrosion* 53, 10 (1997): p. 755-761.
12. P. Jakupi, J.J. Noel, D.W. Shoesmith, *Corros. Sci.* 53, 10 (2011): p. 3122-3130.
13. F.J. Martin, P.M. Natishan, K.E. Lucas, E.A. Hogan, A.M. Grolleau, E.D. Thomas, *Corrosion* 59 (2003): p. 498-504.
14. B.A. Shaw, P.J. Moran, P.O. Gartland, *Corros. Sci.* 32, 7 (1991): p. 707-719.
15. F.J. Martin, K.E. Lucas, E.A. Hogan, *Rev. Sci. Instrum.* 73 (2002): p. 1273.
16. A. Stenta, "One Dimensional Approach to Modeling Damage Evolution in Galvanic Corrosion" (Master's thesis, University of Akron, 2013).
17. A. Stenta, S. Basco, A. Smith, C.B. Clemons, D. Golovaty, K.L. Kreider, J. Wilder, G.W. Young, R.S. Lillard, *Corros. Sci.* 88, 11 (2014): p. 36-48.
18. A. Turnbull, J. Thomas, *J. Electrochem. Soc.* (1982): p. 1412-1422.
19. A. Turnbull, *Mater. Sci. Technol.* 1 (1985): p. 700-710.
20. S.M. Sharland, *Corros. Sci.* 27, 3 (1987): p. 289-323.
21. S.M. Sharland, *Corros. Sci.* 28, 6 (1988): p. 621-630.
22. S.M. Sharland, *Corros. Sci.* 33, 2 (1992): p. 183-201.
23. J.C. Walton, *Nucl. Chem. Waste Manage.* 8, 2 (1988): p. 143-156.
24. J.C. Walton, *Corros. Sci.* 30, 8 (1990): p. 915-928.

25. J.C. Walton, G. Cragnolino, S.K. Kalandros, *Corros. Sci.* 38, 1 (1996): p. 1-18.
26. G.R. Engelhardt, L.G. McMillion, D.D. Macdonald, *J. Nucl. Mater.* 379, 1-3 (2008): p. 48-53.
27. R.G. Kelly, K.C. Stewart, "Combining the Ohmic Drop and Critical Crevice Solution Approaches to Rationalize Intermediate Attack in Crevice Corrosion," in *Passivity of Metals and Semiconductors*, eds. M.B. Ives, J.L. Luo, J.R. Rodda, PV 99-42 (Pennington, NJ: ECS, 2001), p. 546.
28. D.M. Salgado, R.S. Lillard, "On the Mechanism of Damage Evolution During Crevice Corrosion of Alloy 625," CORROSION 2015, paper no. 6552 (Houston, TX: NACE International, 2015).
29. "OLI Systems, Inc.," OLI Systems, 2015.
30. M.D. Brackman, C.B. Clemons, D. Golovaty, K.L. Kreider, J. Wilder, G.W. Young, J. Payer, R.S. Lillard, *J. Electrochem. Soc.* 161, 5 (2014): p. C237-C245.
31. J. Srinivasan, R.G. Kelly, *Corrosion* 70, 12 (2014): p. 1172-1174.
32. A. Stenta, *"Species-Dependent Modeling of Crevice Corrosion Systems"* (Ph.D. thesis, The University of Akron, 2015).
33. A.S. Agarwal, U. Landau, J.H. Payer, *J. Electrochem. Soc.* 155, 5 (2008): p. C269-C278.